NIPPON STEEL TECHNICAL REPORT No. 130 MARCH 2024

Technical Report

Development of Large Cross-section H-shapes and New Structural Design Methods for Steel Beams

Satoshi KITAOKA*
Satoru HIROSHIMA
Masato NIKAIDO
Yusuke SUZUKI
Shun YOSHIMOTO
Hiroshi ITO

Abstract

Recent buildings are characterized by progressively increasing height and large spans. Therefore, large section beams are typically required in those buildings. Based on this need, Nippon Steel Corporation has developed and commercialized the world's largest H-shape product, MEGA NSHYPERBEAM™. New structural design methods for MEGA NSHYPERBEAM have also been developed in order to optimize the cross-section size and to enhance the seismic performance preventing lateral buckling and beam-end fracture. This paper presents an overview of the MEGA NSHYPERBEAM product and its design methods.

1. Commercialization of MEGA NSHYPER BEAM™

1.1 Background of development

Nippon Steel Corporation established a process of rolling H-shaped beams with a web height of up to 1 200 mm and much larger than the manufacturing range of conventional H-shaped beams. In 2020, we started the manufacture and sale of MEGA NSHYPER BEAM™ H-shaped beams in sizes larger than those of NSHYPER BEAM™ (H-shaped beams with constant outer dimensions). To meet further market needs, we increased the flange width to a maximum of 500 mm in 2021. MEGA NSHYPER BEAM™ is produced at a wide flange beam mill in the Wakayama Area (Sakai) of the Kansai Works. The mill began its operation in 1961 as the first of its kind in Japan to use a universal mill. It has developed H-shaped beams with the world's largest thickness, hat-shaped steel sheet piles, and many other new products ahead of other mills. The development of an epoch-making manufacturing process led to the manufacture and sale of NSHYPER BEAM™ in 1989. The outside dimensions or the web height and flange width of NSHYPER BEAM™ were held constant to simplify its design and save on its manufacturing labor. The size menu of NSHYPER BEAM™ has been gradually increased and customers have highly rated the abundant variations, excellent shape and dimensional accuracy, and accurate delivery of NSHYPER BEAM™. NSHYPER BEAM™ is now widely used in buildings for various applications, including superhigh-rise buildings and large logistics facilities.

1.2 Overview of products

Table 1 shows the available sizes of NSHYPER BEAM™ and MEGA NSHYPERBEAM™ and **Table 2** shows the shape and dimensional tolerances of MEGA NSHYPERBEAM™. Assuming use in large buildings such as superhigh-rise buildings, JIS G 3136 SN490B is adopted as the manufacturing standard for MEGA NSHYPERBEAM™. MEGA NSHYPERBEAM™ can be produced in a total of 30 series with a web height range of 800 to 1 200 mm and a flange width range of 300 to 500 mm. We have accepted specific inquiries for the entire range of manufacturable sizes and have tallied the production records. We plan to closely examine market needs, set constantly manufacturable sizes, and strengthen our ability to meet the delivery and other requirements of our customers. The fillet radius (r) of MEGA NSHYPERBEAM™ is set at 30 mm for shape stability as compared with 18 mm for NSHYPER BEAM™. To comply with the strict steel frame production requirements based on the Architectural Institute of Japan's "Japanese Architectural Standard Specification for Steel Work JASS6", MEGA NSHYPERBEAM™ has strict shape and dimensional tolerances specified as done for NSHYPER BEAM™.

2. Development of New Lateral Buckling Design Method for Large Span Beams

2.1 Background of development

In 2017, Nippon Steel developed a lateral bracing elimination

* General Manager, Head of Dept., Dr. Eng., Building Products Engineering Dept., Construction Products Development Div., Plate & Construction Products Unit
2-6-1 Marunouchi, Chiyoda-ku, Tokyo 100-8071

Table 1 Cross-section size of MEGA NSHYPERBEAM

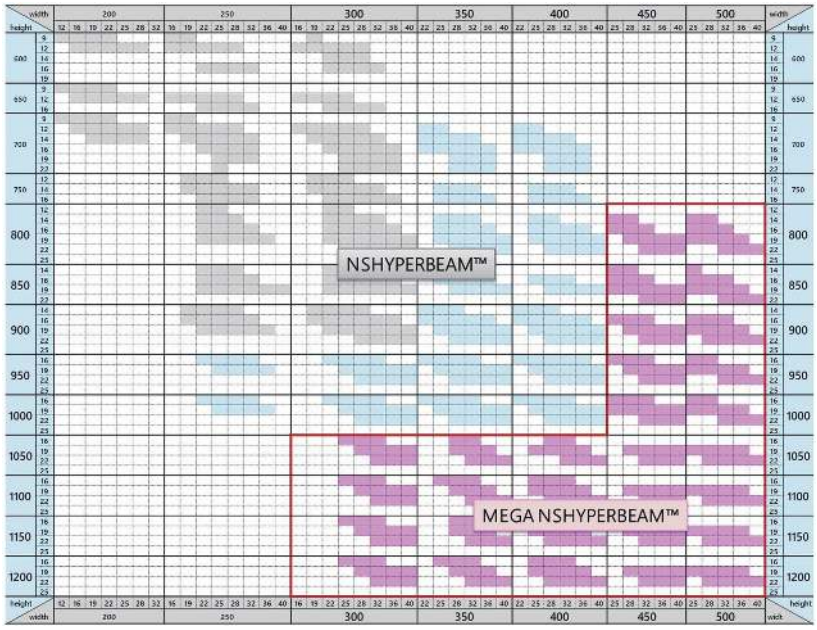

Table 2 Dimensional and shape tolerances

Division			MEGA NSHYPERBEAM mm	JASS6	Apply
B Width		≦400mm	±2.0	±2.0	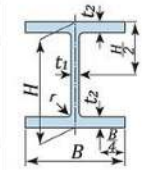
		>400mm	±2.0	±2.0	
H Height		≦800mm, ≦1000mm	±2.0	±3.0	
		>1000mm	±3.0		
Thickness	t2	<16mm	−0.3 +1.7	–	
		≧16mm, <25mm	−0.7 +2.3		
		≧25, <40mm			
		≧40mm	−1.5 +2.5		
	t1	<16mm	±0.7	–	
		≧16mm, <25mm	±1.0		
		≧25mm, <40mm	±1.5		
Length		≦7m	+40 −0	–	
T Squareness			≦2.0	–	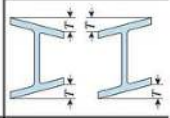
Bend			≦0.10%	≦0.10%, ≦10mm	Up/down, left/right bending
S Eccentricity			±2.0mm	–	$S=\frac{b_1-b_2}{2}$ 
w Concavity ofweb			≦3.0mm	t1>6mm ; ≦H/150, ≦4mm	
F Flange fold			F≦b/100, F≦1.5mm	Joint part ; F≦b/100, F≦1.0	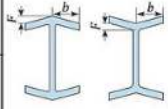
				General ; F≦2b/100, F≦2.0	
E Squareness			≦1.68/100, ≦1.6H/100, e≦3.0mm	–	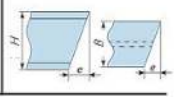

method (hereinafter simply referred to as the method). The method allows the elimination of conventionally used lateral bracing from beams by use of a seismic design technique that considers the effect of floor slabs that restrains the lateral buckling of beams. The method is now being adopted for buildings with a floor area of 2 to 3 million m^2/year and mainly for buildings constructed with NSHYPER BEAM™, such as large logistics facilities. Many urban redevelopment projects are stably conducted under way in the Tokyo metropolitan area and major regional cities. There are active plans to construct new buildings such as data centers and ultra-large factories. These buildings require the use of longer beam spans for improvement in internal space usability and productivity. Against this background, Nippon Steel developed new lateral buckling design method suitable for the design of long-span beams and acquired a building performance certificate from the General Building Research Corporation of Japan (GBRC) in 2020.

2.2 Outline of new lateral buckling design method

When the horizontal movement of the top flange of a beam is restrained by a floor slab, a vertical load such as the weight of the floor slab or the load on the floor slab acts at the midspan of the beam and improves the lateral buckling strength of the beam under an earthquake. The new lateral buckling design method are used to verify the safety of the beam against lateral buckling by considering the effect of the vertical load.

2.2.1 Elastic buckling strength

Equation (1) is used to calculate the elastic lateral buckling moment M^* for primary design when end moment, shear force, and vertical uniformly distributed load act with a constant ratio on a beam with the lateral movement of the top flange constrained by the floor slab. M^* can be obtained by applying the principle of minimum potential energy to the beam system in **Fig. 1**.

$$M^* = \frac{1}{(1-\beta-\gamma)A+(\beta+\gamma)C+\gamma D}\left(B\frac{2\pi^2 EId_b}{L^2}+A\frac{GJ}{d_b}\right) \quad (1)$$

where β and γ are coefficients representing the bending moment distribution of the beam (**Fig. 2**). For example, when checking the residual capacity for the constant load of a beam in a seismically isolated building, the values of β and γ are determined by Eqs. (2) and (3) from the bending moment distribution of the beam obtained by frame analysis, etc.

$$\beta = 1-\frac{M_0}{M_1},\ \gamma = \frac{wL^2}{2}\frac{1}{M_1} \quad (2, 3)$$

where w is the value of the vertical uniformly distributed load acting on the beam per unit length. A, B, C, D, and E are the functionals of the torsion angle ϕ of the beam due to lateral buckling and are expressed by Eqs. (4) to (8), respectively. M_0 and M_1 are bending moments acting on the left and right ends of the beam. Let negative bending be positive. Then, $M_0 \le M_1$. In Fig. 1, M^* is M_1 when the beam buckles laterally.

$$A = L\int_0^L \phi'^2 dz,\ B = \frac{L^3}{2\pi^2}\int_0^L \phi''^2 dz,\ C = \int_0^L z\phi'^2 dz \quad (4\text{–}6)$$

$$D = \frac{2}{L}\int_0^L\int_0^z (z-t)\phi'^2 dt dz,\ E = A-C-D \quad (7, 8)$$

Equation (9) is used to determine the elastic lateral buckling moment M_e^* against a horizontal load such as a seismic force when the vertical uniformly distributed load w is taken as a fixed load. That is, the end load is a variable and w is fixed as an independent variable. Substitution of Eq. (3) into Eq. (1) and equality transformation yield the following equation:

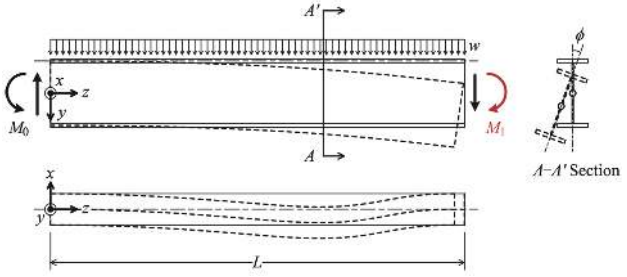

Fig. 1 Analysis model and symbols

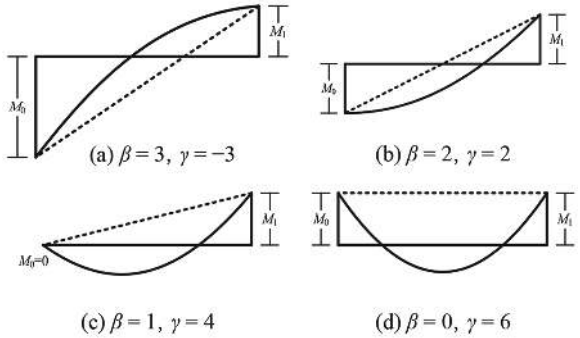

Fig. 2 Moment distribution of beams

$$M_e^* = \frac{1}{(1-\beta)A+\beta C}\left(B\frac{2\pi^2 EI}{L^2}d_b + A\frac{GJ}{d_b} + E\frac{wL^2}{2}\right) \quad (9)$$

In Fig. 1, M_e^* is M_1 when the beam buckles laterally.

2.2.2 Lateral buckling slenderness ratio

When the effect of the vertical load w is considered, the lateral buckling slenderness ratio λ_b^* of a beam with a floor slab can be calculated by Eq. (10). The symbol w is the fixed load directly supported by the beam and β is set to 2 by assuming the bending moment distribution when plastic hinges are formed at the ends of the beam in the ultimate condition. The λ_b^* calculated in this way is taken as the ratio of M_p to the elastic lateral buckling strength M_e^* under corresponding load conditions when the beam ends reach M_p. In other words, λ_b^* can be used as an index when the beam strength and deformation capacity that depend on lateral buckling are estimated by considering the vertical uniformly distributed load.

$$\lambda_b^* = \sqrt{M_p/M_e^*} \quad (10)$$

2.2.3 Approximation of lateral buckling deformation

A, B, C, D, and E in Eqs. (4) to (8) are all the quantities that depend only on the torsion angle ϕ (see Fig. 1) caused in the beam by lateral buckling. When the correct torsion angle ϕ caused in the beam during lateral buckling is substituted into Eqs. (4) to (8), M^* and M_e^* can be obtained as the minimum values of Eqs. (1) and (9), respectively. Because the correct torsion angle ϕ is not known except when a uniform bending moment acts on the beam, ϕ is approximated in series form by Eqs. (11) and (12). The following analytical solutions are obtained by a direct solution method:

$$\text{When } M_0 \neq M_1,\quad \phi = a_0 + \sum_{n=1}^{3} a_n \cos\left\{2\pi\left(\frac{z}{L}\right)^n\right\} \quad (11)$$

$$\text{When } M_0 = M_1,\quad \phi = a_0 + \sum_{n=1}^{3} a_n \cos\left\{\pi\left(\frac{2z}{L}-1\right)^n\right\} \quad (12)$$

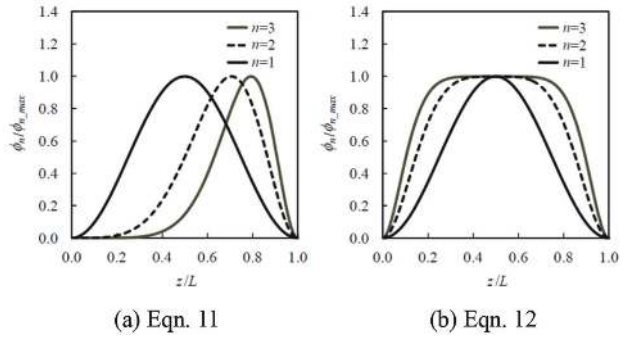

Fig. 3 Basis functions of Eqns. 11 and 12

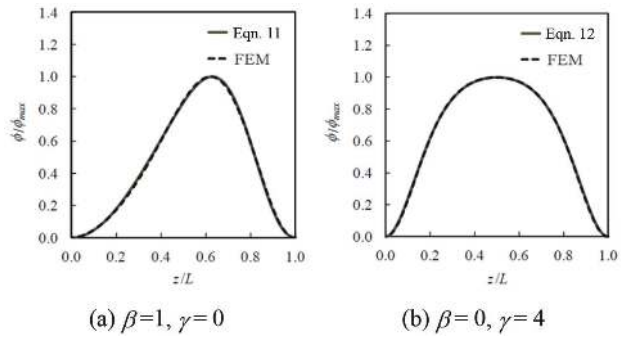

Fig. 4 Comparison of Eqns. 11, 12, and FEM Analyses

As shown in **Fig. 3**, each of the basic functions in Eqs. (11) and (12) is a cosine function when the wavelength is fixed and the phase is an exponential function of the coordinate values in the axial direction of the beam. These finite series approximate ϕ as partial sums up to the third term at most. As shown in **Fig. 4**, the ϕ calculated by Eq. (11) or (12) converges early and can accurately reproduce the ϕ by the FEM elastic buckling analysis when an appropriate value is given for the undetermined coefficient a_n. M^* and M_e^* can be calculated as solutions of cubic equations by solving the minimum conditions of Eqs. (11) and (12) for the undetermined coefficient a_n.

2.2.4 Verification of accuracy of M^*

Derivation of the analytical solution by a direct method is an upper approximation that assumes buckling deformation. The accuracy of the analytical solution depends on the correctness of the assumed ϕ (how close it is to the correct ϕ). Elastic buckling analysis by FEM is thus performed to verify M^* by Eq. (1). The analysis cases are shown in **Table 3** and the analysis model is shown in **Fig. 5**. Analysis variables are the beam cross-section, length, and loading conditions (β and γ mentioned above). The beam end moment M_{FEM} on the negative bending side of the first-order buckling mode is extracted for 2304 cases. As shown in **Fig. 6**, M^* agrees well with M_{FEM} when lateral buckling is dominant. In other words, Eq. (1) can accurately estimate the elastic lateral buckling strength of a beam whose lateral movement is restrained, regardless of its cross-section, length, and loading conditions.

2.2.5 Verification of accuracy of λ_b^*

FEM elasto-plastic analysis is performed with the analysis model as in the previous section to verify λ_b^* when M_e^* from Eq. (9) is used. **Table 4** shows the analysis cases. **Figure 7** shows the initial imperfection given to the analysis model. **Figure 8** shows the stress-strain relationships used in the analysis. The initial imperfection is obtained by superimposing the primary mode of lateral buckling (Fig. 7(a)) obtained by elastic buckling value analysis and the primary mode of local buckling at the beam end (Fig. 7(b)). The size of the initial imperfection is set so that the maximum value of the nodal displacement in each mode becomes 1/2000 of the beam depth. The nominal stress-nominal strain relationship (dotted line in Fig. 8) is modeled by the modified Menegotto-Pinto model and is replaced by the true stress-logarithmic strain relationship (solid line in Fig. 8). The stress-strain relationship is approximated by a polyline. The yield strength is 358 MPa and the tensile strength is 490 MPa. In the analysis, a given w is applied to a beam with both ends

Table 3 Analysis cases

Beam (SN490B)		Loading condition	
Cross-section	L/H	β	γ
H-400×400×13×21	6–100	3	0
H-588×300×12×20		2	$2-\beta/3$
H-600×200×11×17		1	$4-2\beta/3$
		0	$6-2\beta$

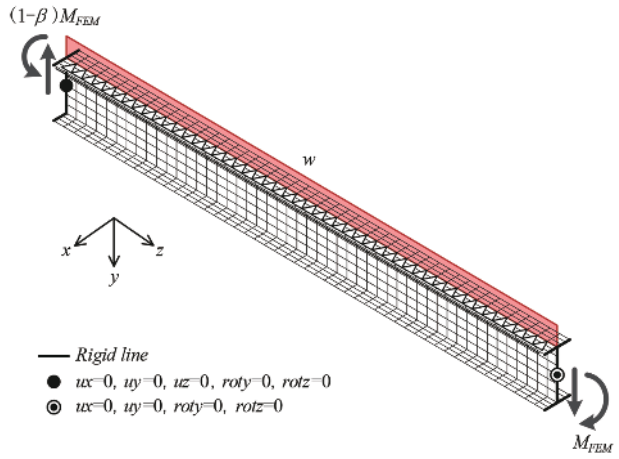

Fig. 5 Analysis model

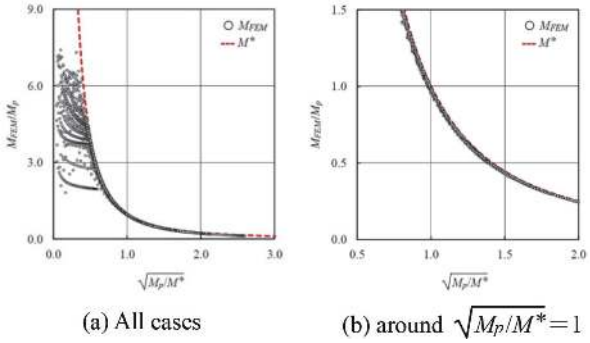

Fig. 6 Comparison of M^* and FEM analysis

Table 4 Analysis cases

Beam (SN490B)		w
Cross-sectional	L/H	kN/m
H-588×300×12×20	12–40	0, 10

fixed to constrain the lateral movement of the top flange. Antisymmetric rotation angles are applied to the left and right ends of the beam while maintaining a constant load. The analysis variables are the cross-section and length of the beam, and the presence or absence of w. The relationship between the beam end moment on the negative bending side and the beam end rotation angle is obtained. The maximum strength M_{FEM} and the plastic ductility η_{FEM} are extracted as the analysis results.

Figure 9 shows the analysis results. Both the M_{FEM}/M_p–λ_b* and η_{FEM}–λ_b* relationships are almost the same with and without w. In other words, by using M_e* from Eq. (9), λ_b* can evaluate the lateral buckling-dependent yield strength and deformation capacity of the beam by considering the effect of the vertical uniformly distributed load.

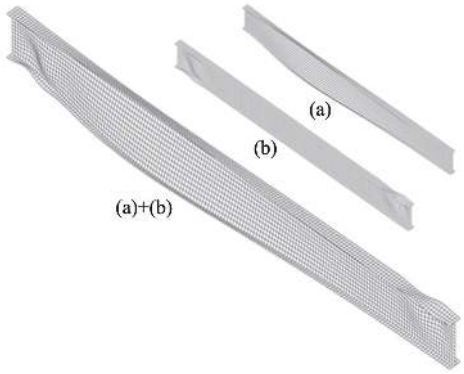

Fig. 7 Initial imperfection

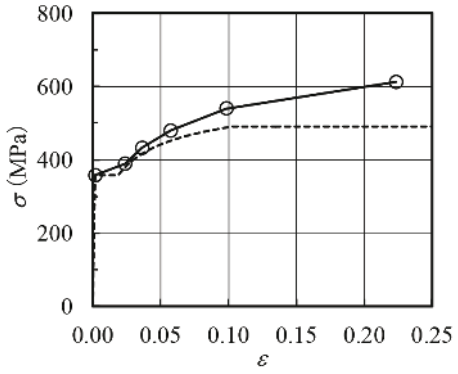

Fig. 8 Stress-strain relationship

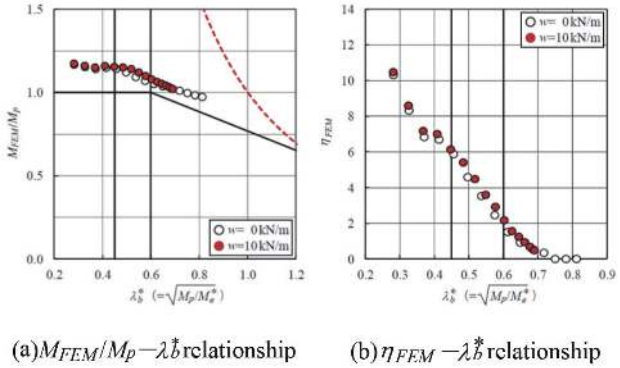

Fig. 9 FEM analysis results

3. Development of Haunchless Beam End Method (Inverted Scallop Method)

3.1 Background of development

Weld access holes or scallops are cut out at beam web ends for on-site welding of beam flange ends. The haunchless beam end method (inverted scallop method) prevents the premature fracture of beam end flange welds from originating from the strain concentration at the bottom of scallops by reviewing the shape of the scallops. In the 1994 Northridge Earthquake in the United States and the 1995 Hyogo-ken Nanbu Earthquake in Japan, premature fractures of beam end flange welds[1–3] were confirmed as examples of damage to steel frame structures in epicentral earthquakes. Consequently, a composite circular scallop method and a haunching beam flange method have been proposed and implemented in Japan. In the former method, a curve with a radius of about 10 mm is provided at the bottom of a scallop to relieve the strain concentration there. In the latter, the ends of a beam are widened in the beam width direction. Furthermore, in the 2011 off the Pacific Coast of Tohoku Earthquake, long-period and long-duration ground motions were observed. The safety of structures against such ground motions was not fully verified in conventional seismic design. Industry, government, and academia are jointly developing design methods to prevent the fracture of beam end flange welds.[4] Against this background, Nippon Steel, Nikken Sekkei Ltd., and Nagai Seisakusho Co., Ltd. jointly developed the haunchless beam end method (inverted scallop method) and are now applying it to actual construction projects.

3.2 Overview of method

In the haunchless beam end method (inverted scallop method), the scallop shape is changed to the inverted scallop shown in **Fig. 10** to alleviate the strain concentration at the scallop bottom and prevent premature fracture of the beam end flange weld from originating from the scallop bottom. The shape of the inverted scallop is a conventional composite circular scallop turned almost upside down. A straight line, an approximately quarter circle with a radius r_1 of about 6 mm, and an approximately quarter circle with a radius r_2 of about 35 mm are combined to smoothly shape the scallop bottom. In addition, the scallop bottom is raised about 6 mm (d_0) in the web height direction to alleviate the strain concentration at the scallop bottom. Scallops are machined with a five-side cutting machine (**Photo 1**) or with a cutter (**Photo 2**) on an H-shaped beam beveling machine. When using an H-shaped beam beveling machine, scallops can be machined with an inverted scallop cutter (**Photo 3**) in place of the conventional composite circular scallop cutter.

3.3 FEM analysis

FEM elasto-plastic analysis was performed to verify the effect of the scallop shape on the strain concentration at the scallop bottom (**Fig. 11**). The analysis model is a through-diaphragm type T-shaped partial frame. The analysis variable is scallop shaped. Two types of

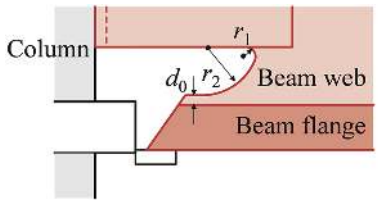

Fig. 10 The inverted scallop

scallops, or a composite circular scallop and an inverted scallop, are analyzed. The loading method is monotonic loading in which forced displacement is applied at the beam end in one direction.

Figure 12 shows the equivalent plastic strain distribution around the scallop when the member angle of the beam is 1/30 rad. The composite circular scallop has an equivalent plastic strain largely concentrated at the scallop bottom. On the other hand, it can be confirmed that the equivalent plastic strain at the bottom of the inverted scallop is smaller than that of the composite circular scallop.

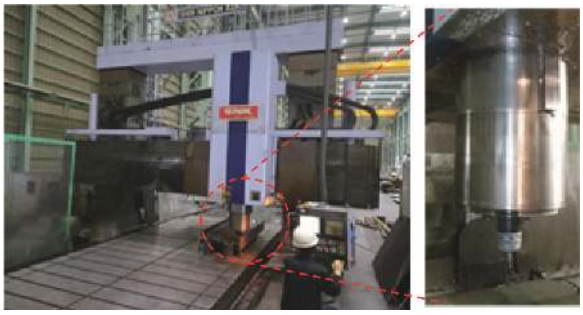

Photo 1 Five-sided processing machine

Photo 2 Five-sided processing machine for H-shapes

Photo 3 Cutter for the inverted scallop

3.4 Full-scale test

To investigate the fracture process leading to the fracture of beam end connections welded by using inverted scallops and the cyclic deformation performance of beam end connections, through-diaphragm beam end connections were tested under constant amplitude cyclic loading. SN490B beams and BCP325B square steel pipe columns were used in the test. As shown in **Table 5**, the test speci-

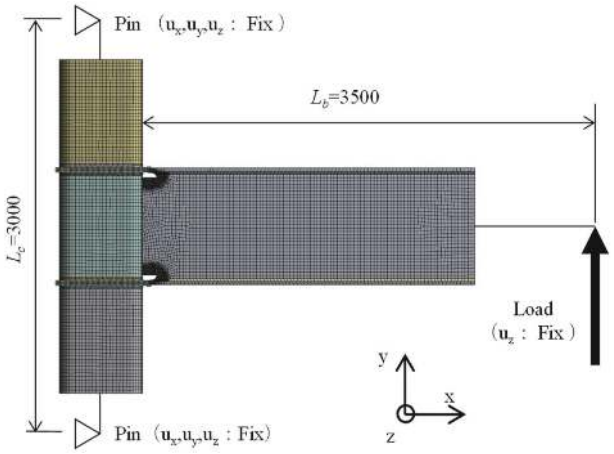

Fig. 11 FEM analysis model

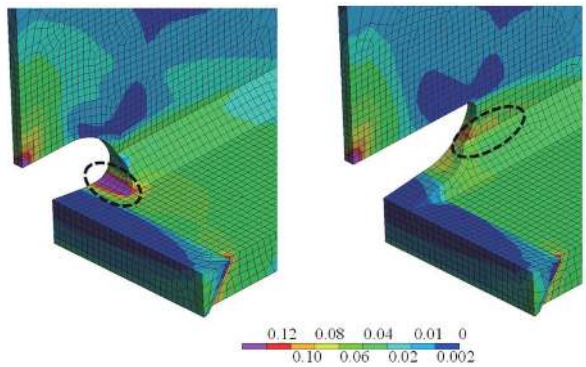

(a) Composite circular scallop (conventional) (b) Inverted scallop

Fig. 12 Distribution of equivalent plastic strain

Table 5 Specimen list

Series	No.	Beam [SN490B]	Column [BCP325B]	Scallop	Frange groove orientation	SAW $_vE_0$ (J)*	Amplitude (θ_p)	$_jM_u/_bM_p$
1	No.1	BH-700×200×12×22	□−500×22	Inverted	Inside	91	3	1.18
	No.2	BH-700×200×12×28	□−500×22			92		1.24
	No.3	BH-700×200×12×22	□−500×22		Outside	91		1.18
	No.4	BH-700×200×12×25	□−500×19			106		1.30
	No.5	BH-700×200×12×22	□−500×22	Composite circular (conventional)	Inside	91		1.18
2	No.6	BH-700×200×12×25	□−500×19	Inverted	Inside	20	1.2	1.30
	No.7	BH-700×200×12×22	□−500×22			91	1.2	1.18
	No.8	BH-700×200×12×25	□−500×19			20	2	1.30

* Results of Charpy impact test @0°C

mens were designed so that the ratio of the total plastic moment ${}_bM_p$ of the beam to the maximum bending strength ${}_jM_u$ of the beam end connection became 1.18 to 1.30. The test variables are scallop shaped (inverted or composite circular), flange groove orientation (inside or outside), and loading amplitude. Non-metal end tabs were used as the end tabs for beam end flange welds, and 550N grade solid wire (JIS Z 3312 YGW18) was used as the welding material. Specimens were cyclically loaded with constant amplitude (**Fig. 13**). Specimen columns were pin supported at both ends. A hydraulic jack was horizontally connected to the beam end through a load cell. To prevent the beam from deforming out of the structural plane, the beam was constrained at one point by a pantograph. The elastically calculated beam member angle ${}_b\theta_p$ when the beam end reaches ${}_bM_p$ was taken as the reference displacement. The single amplitude of the cyclic loading was set to $1.2{}_b\theta_p$, $2{}_b\theta_p$, and $3{}_b\theta_p$.

3.5 Test results

Beam end connection fracture modes are schematically illustrated in **Fig. 14**. Typical ultimate states of specimens are shown in **Photo 4**. None of the specimens buckled locally. Each specimen decreased in strength due to fracture of the beam end flange weld and ended the test. The test confirmed the presence of the crack C_s originating from the bottom of the scallop and the cracks C_{f1} and C_{f2} originating from the weld toe and weld root at the weld start and end positions of the beam flange weld, respectively. In specimens No. 1 and No. 2 with inverted scallops and inside groove, the flange fractured at the crack C_{f2} at the weld toe on the inner surface of the beam end flange weld (Fig. 14(a), Photo 4(a)). In specimens No. 3 and No. 4 with inverted scallops and outside groove, the flange fractured at the crack C_{f1} at the weld toe on the outer surface of the beam end flange weld (Fig. 14(b), Photo 4(b)). In the No. 5 specimen with a composite circular scallop used, the flange fractured at the crack C_s at the scallop bottom (Fig. 14(c), Photo 4(c)). Specimens Nos. 6 to 8 fractured at the crack C_{f2} formed at the weld toe position on the inner side of the flange end, regardless of the toughness of the flange-web Submerged-Arc Welding (SAW) metal and the loading amplitude. The test confirmed that the fracture originating from the scallop bottom was suppressed in the beam end connection welded by using an inverted scallop and that the flange fracture originated from the ductile crack at the weld toe of the beam flange end.

Table 6 lists the test results. **Figure 15** shows the examples of the load-deformation relationships of some specimens. Fracture modes can be roughly divided into two types: brittle fracture and ductile fracture. Brittle fracture is defined as a fracture that occurs without significant strength degradation during loading, and the area of ductile cracks on the fracture surface is small compared to the total area. Ductile fracture is defined as a fracture that occurs as the strength decreases with increasing loading cycles, and the area of ductile cracks on the fracture surface is large compared to the total area. The number of cycle to fracture N_f (hereinafter referred to as fracture life) is defined as the number of cycles when either flange fractures, the number of cycles when the peak load is reached before the half-cycle maximum member angle is reached, or the final number of cycles when the half-cycle peak load accounts for 50% or more of the maximum peak load, whichever is smallest. **Figure 16** shows the fracture life N_f on the horizontal axis and the ductility fac-

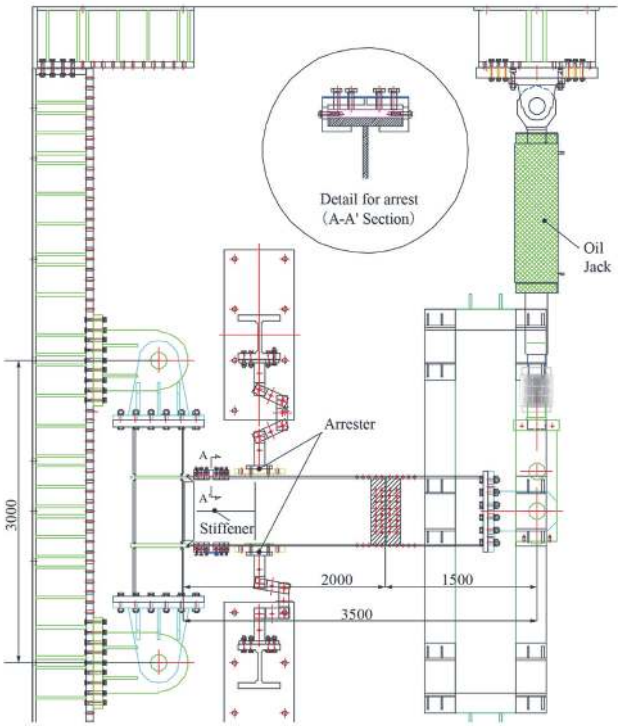

Fig. 13 Test set-up and loading condition

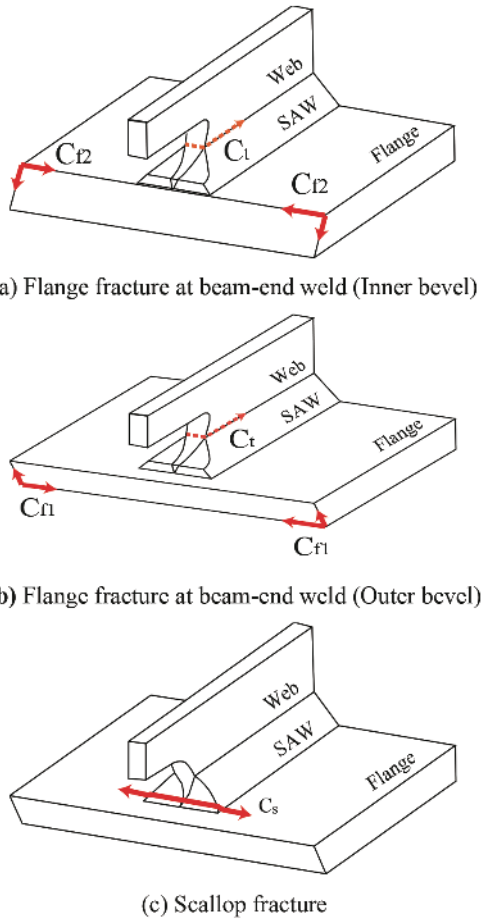

Fig. 14 Mode of beam-end fracture

tor μ on the vertical axis. The dashed, dotted, and solid lines respectively represent the empirical equation (C=5.6) and the design equation (C=7.0) for beam end connections welded without scallops in the low-cycle fatigue curve[5] shown in Eq. (13) and the design equation (C=5.4) for evaluating beam end connections welded by using inverted scallops. We can confirm that specimens with inverted scallops are superior in cyclic deformation performance to specimens with composite circular scallops and can exhibit cyclic deformation performance roughly equivalent to that of specimens without scallops. The inverted scallop method also has the cross-section reduced by the scallops. With the lateral stiffener elimination method discussed above, as a measure for evaluating the test results on the safe side, the design C value is set to 5.4 so that the actual cyclic deformation performance becomes about 70% of the minimum test cyclic deformation performance.

$$\mu = C \cdot N_f - \beta \quad (13)$$

(a) No. 1 : Flange fracture at beam-end weld

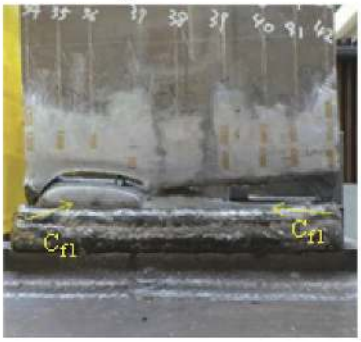

(b) No. 3 : Flange fracture at beam-end weld

(c) No. 5 : Flange fracture at beam-end weld scallop

Photo 4 Specimens after the experiment

where C is a fracture life coefficient and β is the slope (= 1/3) of the evaluation equation.

Table 6 Experimental data

No.	Weld hole	Amplitude (θ_p)	${}_jM_u / {}_bM_p$	Fracture point	Fracture type	N_f
No.1	Inverted scallop	3	1.18	Flange weld line	Ductile	17
No.2			1.24	Flange weld line	Ductile	25
No.3			1.18	Flange weld line	Ductile	8
No.4			1.30	Flange weld line	Ductile	17
No.5	Composite circular scallop (conventional)		1.18	Near the scallop	Brittle	2
No.6	Inverted scallop	1.2	1.30	Flange weld line	Ductile	342
No.7		1.2	1.18	Flange weld line	Ductile	162
No.8		2	1.30	Flange weld line	Ductile	49

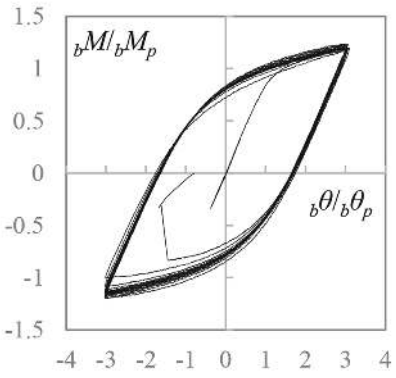

(a) No. 1 : Fracture point : Flange weld line

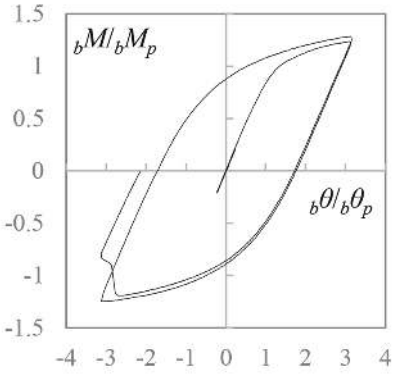

(b) No. 5 : Fracture point : Near the scallop

Fig. 15 Load-displacement relationships

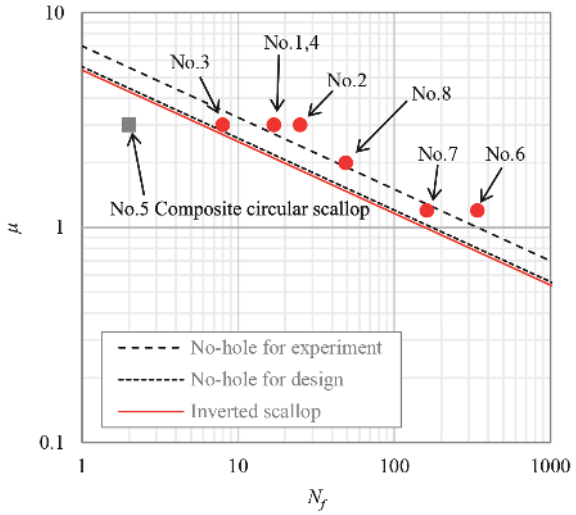

Fig. 16 Plasticity-fatigue performance relationship

3.6 Application to actual projects

The study results concerning the beam end connections welded by using inverted scallops were summarized as design and construction guidelines. In 2021, the Building Center of Japan evaluated the design and construction guidelines. We have started to apply the design and construction guidelines to construction projects such as high-rise buildings.

4. Conclusions

In this paper, we have outlined MEGA NSHYPERBEAM™ products and described the long-span beam horizontal buckling design method and on-site beam end welding technology we have developed. MEGA NSHYPERBEAM™ and these design and construction technologies can be combined to reduce the weight of long-span beams and to save the labor required for steel frame fabrication and on-site construction. We will focus on the rapid spread and stable supply of MEGA NSHYPERBEAM™ and will take the initiative to develop new environmentally friendly construction methods toward a decarbonized society.

References

1) Steel Committee of Kinki Branch, the Architectural Institute of Japan: Reconnaissance Report on Damage to Steel Building Structures Observed from the 1995 Hyogoken-Nanbu (Hanshin/Awaji) Earthquake, 1995.5
2) Architectural Institute of Japan: Damage and Lessons of Steel Structures in the Hyogoken-nanbu Earthquake, 1996.7
3) Japanese Society of Steel Construction: Report on Investigation of Damage to Steel Frame Buildings in Southern Hyogoken-nanbu Earthquake, 1997.2
4) Architectural Institute of Japan, Steel Construction Steering Committee, Architectural Institute of Japan: Proceedings of Research Results Meeting, Chapter 3 - Scallop WG, p. 89–164, 2000.11
5) Hasegawa, T., Fukumoto, T., Tagami, J., Sawamoto, Y., Kubota, J., Tokinoya, H., Suzui, Y., Terada, T., Ishii, D., Narihara, H., Yasuda, S., Kaneko, H., Usami, T., Koshika, N., Suzuki, Y., Nishiyama, I., Mukai, A., Iwata, Y.: Study on Seismic Performance for Super-High-Rise Steel Buildings against Long-Period Earthquake Ground Motions, Building Research Data No.160, Building Research Institute, 2014.7

Satoshi KITAOKA
General Manager, Head of Dept., Dr. Eng.
Building Products Engineering Dept.
Construction Products Development Div.
Plate & Construction Products Unit
2-6-1 Marunouchi, Chiyoda-ku, Tokyo 100-8071

Yusuke SUZUKI
Chief Manager, Head of Section, Ph.D.
Building Products Engineering Section-I
Building Products Engineering Dept.
Construction Products Development Div.
Plate & Construction Products Unit

Satoru HIROSHIMA
Researcher
Research Section-II
Steel Structures Research Dept.-II
Steel Structures Research Lab.
Steel Research Laboratories

Shun YOSHIMOTO
Building Products Engineering Section-I
Building Products Engineering Dept.
Construction Products Development Div.
Plate & Construction Products Unit

Masato NIKAIDO
Senior Researcher
Research Section-I
Steel Structures Research Dept.-II
Steel Structures Research Lab.
Steel Research Laboratories

Hiroshi ITO
Chief Manager, Head of Section, Dr.(Eng.)
Building Products Engineering Section
Construction Products Engineering Dept.
Osaka Office